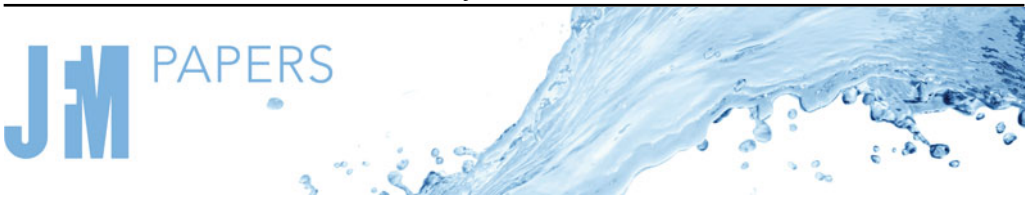
J. Fluid Mech. (2026), *vol.* 1031, A10, doi:10.1017/jfm.2026.11252



Theoretical modelling for bubble dynamics with migration effects under dynamic Reynolds numbers

Run-Ze Xu[1], **A-Man Zhang**[1,2,3], **Shi-Min Li**[1,2] **and Shi-Ping Wang**[1,2,3]

[1]College of Shipbuilding Engineering, Harbin Engineering University, Harbin 150001, PR China

[2]National Key Laboratory of Ship Structural Safety, Harbin Engineering University, Harbin 150001, PR China

[3]Nanhai Institute of Harbin Engineering University, Sanya 572024, PR China

Corresponding author: A-Man Zhang, zhangaman@hrbeu.edu.cn

(Received 28 June 2025; revised 22 January 2026; accepted 23 January 2026)

Bubble dynamics constitutes a fundamental scientific problem in fluid mechanics. Although the oscillation can be predicted through theories for bubble dynamics in previous studies, the viscous effects on the bubble migration remains difficult to predict accurately. In this study, we establish a theoretical model for bubble migration across the entire cycle. The theoretical model derives a drag coefficient expression under dynamic Reynolds numbers, and incorporates corrections to account for non-spherical bubble dynamics. A key advance is the capability to account for viscous drag without relying on constant empirical drag coefficients. Validation against experimental results demonstrates that the theoretical model effectively predicts the bubble migration. Furthermore, we discuss the correlation between drag coefficient and Reynolds number, and elucidate the effects of viscous domain range and bubble deformation on the drag coefficient of the present model.

Key words: bubble dynamics

1. Introduction

Bubbles are ubiquitous in diverse fluid mediums, including water, oils, bodily fluids, beverages and chemical reagents, such as large-scale oceanic bubbles (De Graaf, Brandner & Penesis 2014; Li *et al.* 2020) and drag-reducing bubbles (Verschoof *et al.* 2016), biological phenomena (Lohse, Schmitz & Versluis 2001), explosion bubbles

© The Author(s), 2026. Published by Cambridge University Press. This is an Open Access article, distributed under the terms of the Creative Commons Attribution licence (https://creativecommons.org/licenses/by/4.0/), which permits unrestricted re-use, distribution and reproduction, provided the original article is properly cited.

https://doi.org/10.1017/jfm.2026.11252 Published online by Cambridge University Press

(Best 1991), vapour bubbles in boiling oil (Mitrovic 1998; Lioumbas & Karapantsios 2015), micro-vacuoles in tissues (Fry *et al.* 1995; Klibanov 2007), pressurised bubbles in carbonated drinks (Vega-Martínez *et al.* 2017; Zenit & Rodríguez-Rodríguez 2018), and bubbles from chemical reactions (Merouani & Hamdaoui 2016; Sabdenov 2020). Across these applications, fluid compressibility and viscosity critically influence bubble dynamics by dissipating energy within the bubble system (Wang 2016; Fang *et al.* 2025*a*,*b*). To elucidate these mechanisms and explore how fluid properties affect bubble behaviour, extensive research has employed a number of theoretical analysis, which has been instrumental in formalising the underlying mechanical principles mathematically.

Theoretical investigations of bubble dynamics have evolved significantly over decades. Assuming incompressible fluids, early foundational work established classical models primarily through modifications of the Rayleigh–Plesset equation (Rayleigh 1917; Plesset 1949), focusing heavily on viscosity effects for bubble oscillation (Plesset 1964; Yang & Yeh 1966; Fogler 1969; Apfel 1981). Subsequently, models were progressively extended to encompass compressible fluids (Gilmore 1952; Keller & Miksis 1980; Ma, Hsiao & Chahine 2018). More recently, Zhang *et al.* (2024) proposed bubble oscillation and migration equations (the Zhang equation) from a potential flow perspective, establishing a multi-factor theoretical model for spherical bubbles. While the Zhang equation incorporates viscosity considerations for bubble migration, its viscous effect is represented through an added drag coefficient (C_d). This approach highlights a persistent challenge: many hydrodynamic models based on potential flow theory (Hicks 1970; Plesset & Prosperetti 1977; Prosperetti & Lezzi 1986; Brujan, Pearson & Blake 2005; Peñas-López *et al.* 2016) inherently struggle to objectively characterise fluid viscosity, necessitating empirical adjustments via drag coefficients. This reliance on phenomenological parametrisation introduces empirical uncertainties, potentially hindering rigorous theoretical exploration of the coupling between bubble oscillation and migration dynamics.

The characterisation of drag coefficients, crucial in migration models, has its own theoretical trajectory. For flow past spherical structures, Aybers & Tapucu (1969) noted that Stokes originally elucidated low-Reynolds-number drag, where a bubble's surface tangential velocity equals half that of a rigid sphere, yielding a viscous drag coefficient of unity under Stokes' assumptions. Later boundary layer analyses for higher Reynolds numbers by Levich (1962) and Moore (1963) aligned with this, deriving $C_d = 48/Re$. However, fundamental limitations arise from the Stokes hypothesis neglecting convective terms, intrinsic constraints of boundary layer theory, and omission of higher-order terms. These simplifications lead to significant discrepancies in applicability and accuracy for drag coefficient implementations, preventing a novel theoretical framework. Furthermore, the migration equation formulations in these studies omitted critical fluid compressibility effects and employed time-independent drag coefficients lacking analytical expressions. Consequently, while partially elucidating parametric dependencies under constrained conditions, these models cannot universally describe diverse bubble behaviours. Numerous other studies have analysed drag in bubbles under various conditions (Roghair *et al.* 2011; Mattson & Mahesh 2011; Ravelet, Colin & Risso 2011; Roig *et al.* 2012; Brujan *et al.* 2022), offering more intuitive and accurate depictions. However, these investigations rely heavily on numerical computation and experimental observation, limiting their direct utility for theoretical development and subsequent research. Moreover, numerical results depend critically on computational precision, and exploring underlying principles demands substantial investment.

This study addresses these limitations by developing a comprehensive theoretical framework for bubble dynamics through the previous framework of Zhang *et al.* (2024),

https://doi.org/10.1017/jfm.2026.11252 Published online by Cambridge University Press

with specific focus on viscous effects under dynamic Reynolds numbers. While the previous framework inherently accommodates fluid compressibility, substantial analytical complexities arise from simultaneous considerations of compressible effects and unsteady flow characteristics during viscous interaction analysis. To circumvent these theoretical impediments, we have simplified the contribution of these factors to viscous effects within the theoretical model. A generalised formulation for the drag coefficient C_d is established for dynamic Reynolds numbers, incorporating the influence of convection terms. By leveraging the continuity of the evolutionary process for extrapolation and subjecting it to rigorous validation across a wide range of bubble experiments, a drag coefficient formula with broad applicability was developed, thereby enhancing the objective characterisation of viscous phenomena within the theoretical framework of the Zhang equation.

The structure of the paper is as follows. For the theoretical model in § 2, § 2.1 derives the velocity and pressure fields for viscous flow around bubble. Building upon this foundation, § 2.2 computes the drag force and drag coefficient acting upon the bubble by introducing a boundary layer to accommodate high-Reynolds-number scenarios. Section 2.3 proceeds to implement corrections for substantial deformations. Then the results based on the model are analysed in § 3. Finally, the conclusions are summarised in § 4.

2. Theoretical model

2.1. *The velocity and pressure field for viscous flow*

While in the viscous fluid, if the body force is neglected, then the velocity and pressure fields are fundamentally governed by the Navier–Stokes equation

$$\frac{\partial \boldsymbol{u}}{\partial t} + \boldsymbol{u} \cdot \nabla \boldsymbol{u} = -\frac{1}{\rho}\nabla p + \frac{\mu}{\rho}\nabla^2 \boldsymbol{u}, \tag{2.1}$$

where ρ and μ are the density and dynamic viscosity coefficient of the fluid, and $\boldsymbol{u}$ and p represent the velocity and pressure of the fluid field, respectively. In accordance with the Helmholtz velocity decomposition theorem, the fluid field can be decomposed into the superposition of an irrotational potential field and a rotational viscous field (Moore 1963; Ai & Ni 2017). Consequently, (2.1) can be further expressed as

$$\frac{\partial}{\partial t}(\boldsymbol{u}_s + \boldsymbol{u}_v) + (\boldsymbol{u}_s + \boldsymbol{u}_v) \cdot \nabla (\boldsymbol{u}_s + \boldsymbol{u}_v) = -\frac{1}{\rho}\nabla (p_s + p_v) + \frac{\mu}{\rho}\nabla^2 (\boldsymbol{u}_s + \boldsymbol{u}_v), \tag{2.2}$$

where $\boldsymbol{u}_s$ and $\boldsymbol{u}_v$ are the velocities of the potential and viscous fields, respectively, and p_s and p_v are the fluid pressures for the potential and viscous fields correspondingly. This decomposition separates the flow into a part that can be described by a potential for irrotational effects and a part accounting for viscous rotational effects. Within the realm of potential fields, the intricate relationship between velocity and pressure is governed by the Euler equation

$$\frac{\partial \boldsymbol{u}_s}{\partial t} + \boldsymbol{u}_s \cdot \nabla \boldsymbol{u}_s = -\frac{1}{\rho}\nabla p_s, \tag{2.3}$$

which governs the motion of an ideal (inviscid) fluid, where the pressure gradient provides the sole force for fluid acceleration. By simultaneously considering (2.2) with (2.3), we obtain

$$\frac{\partial \boldsymbol{u}_v}{\partial t} + \boldsymbol{u}_v \cdot \nabla \boldsymbol{u}_s + (\boldsymbol{u}_s + \boldsymbol{u}_v) \cdot \nabla \boldsymbol{u}_v = -\frac{1}{\rho}\nabla p_v + \frac{\mu}{\rho}\nabla^2 (\boldsymbol{u}_s + \boldsymbol{u}_v), \tag{2.4}$$

https://doi.org/10.1017/jfm.2026.11252 Published online by Cambridge University Press

which constitutes the momentum equation derived through rigorous mathematical derivation from the Navier–Stokes and Euler equations. The equation specifically describes the evolution of the viscous component of the velocity field $\boldsymbol{u}_v$, showing how it is influenced by interactions with the potential flow, its own inertia, and viscous diffusion.

Given the computational complexity arising from multifactorial dependencies in viscous field spatiotemporal resolution, while the Strouhal number for bubble migration satisfies $St \leq 0.3$ generally (Levi 1983; Hanafizadeh *et al.* 2013), coupled with prior incorporation of bubble temporal evolution by Zhang *et al.* (2024), we implement a trapezoidal integration scheme for temporal discretisation. This approach employs a quasi-steady approximation that neglects transient flow effects within discrete temporal increments while preserving spatial gradient influences on viscous fluid dynamics. Under this condition, taking the curl of (2.4) yields

$$\boldsymbol{\nabla} \times [\boldsymbol{u}_v \cdot \boldsymbol{\nabla} \boldsymbol{u}_s + (\boldsymbol{u}_s + \boldsymbol{u}_v) \cdot \boldsymbol{\nabla} \boldsymbol{u}_v] = \frac{\mu}{\rho} \nabla^2 (\boldsymbol{\nabla} \times \boldsymbol{u}_v). \tag{2.5}$$

Taking the curl eliminates the pressure gradient term, focusing the equation on the evolution of vorticity ($\boldsymbol{\nabla} \times \boldsymbol{u}_v$), which is generated and diffused by velocity gradients and viscous effects. By incorporating the principles of tensorial transformation laws, (2.5) may give the subsequent relations with heightened rigour:

$$\begin{aligned} &\boldsymbol{\nabla} \left(\boldsymbol{u}_v \cdot \boldsymbol{u}_s + \frac{1}{2} u_v^2 \right) - \boldsymbol{u}_v \left(\boldsymbol{\nabla} \cdot \boldsymbol{u}_s \right) - (\boldsymbol{u}_s + \boldsymbol{u}_v) \left(\boldsymbol{\nabla} \cdot \boldsymbol{u}_v \right) \\ &+ (\boldsymbol{u}_s + \boldsymbol{u}_v) \cdot \boldsymbol{\nabla} (\boldsymbol{\nabla} \times \boldsymbol{u}_v) = \frac{\mu}{\rho} \nabla^2 (\boldsymbol{\nabla} \times \boldsymbol{u}_v), \end{aligned} \tag{2.6}$$

where u_v^2 means the squared magnitude of $\boldsymbol{u}_v$, i.e. $u_v^2 = \boldsymbol{u}_v \cdot \boldsymbol{u}_v$. Simultaneously, given our heightened focus on viscous effects within the fluid field, and acknowledging the intricate interplay between fluid compressibility and viscous forces, coupled with the observation that bubble Mach numbers remain below 0.3 under most operational conditions (Han, Yan & Li 2024), we proceed under the premise of incompressible fluid dynamics

$$\boldsymbol{\nabla} \cdot (\boldsymbol{u}_s + \boldsymbol{u}_v) = \boldsymbol{\nabla} \cdot \boldsymbol{u}_s = \boldsymbol{\nabla} \cdot \boldsymbol{u}_v = 0, \tag{2.7}$$

which simplifies the analysis by enforcing mass conservation and eliminating dilatational effects. Then substituting (2.7) into (2.6) yields

$$\boldsymbol{\nabla} \left(\boldsymbol{u}_v \cdot \boldsymbol{u}_s + \frac{1}{2} u_v^2 \right) + (\boldsymbol{u}_s + \boldsymbol{u}_v) \cdot \boldsymbol{\nabla} (\boldsymbol{\nabla} \times \boldsymbol{u}_v) = \frac{\mu}{\rho} \nabla^2 (\boldsymbol{\nabla} \times \boldsymbol{u}_v), \tag{2.8}$$

which highlights the balance between the gradient of a kinetic-energy-like term (combining potential and viscous field energies), the convection of vorticity, and the viscous diffusion of vorticity. To nullify the effects of the curl term, we apply the divergence operator to (2.8), thereby obtaining

$$\boldsymbol{\nabla} \cdot \left[\boldsymbol{\nabla} \left(\boldsymbol{u}_v \cdot \boldsymbol{u}_s + \frac{1}{2} u_v^2 \right) + (\boldsymbol{u}_s + \boldsymbol{u}_v) \cdot \boldsymbol{\nabla} (\boldsymbol{\nabla} \times \boldsymbol{u}_v) \right] = 0, \tag{2.9}$$

which yields a scalar equation whose solution can help constrain the velocity field. By applying the tensor transformation relations for the three-dimensional axisymmetric model, it becomes evident that the divergence of $\boldsymbol{u}_v \cdot \boldsymbol{\nabla} (\boldsymbol{\nabla} \times \boldsymbol{u}_v)$ vanishes identically, thereby yielding

$$\boldsymbol{\nabla} \cdot \left[\boldsymbol{\nabla} \left(\boldsymbol{u}_v \cdot \boldsymbol{u}_s + \frac{1}{2} u_v^2 \right) + \boldsymbol{u}_s \cdot \boldsymbol{\nabla} (\boldsymbol{\nabla} \times \boldsymbol{u}_v) \right] = 0, \tag{2.10}$$

https://doi.org/10.1017/jfm.2026.11252 Published online by Cambridge University Press

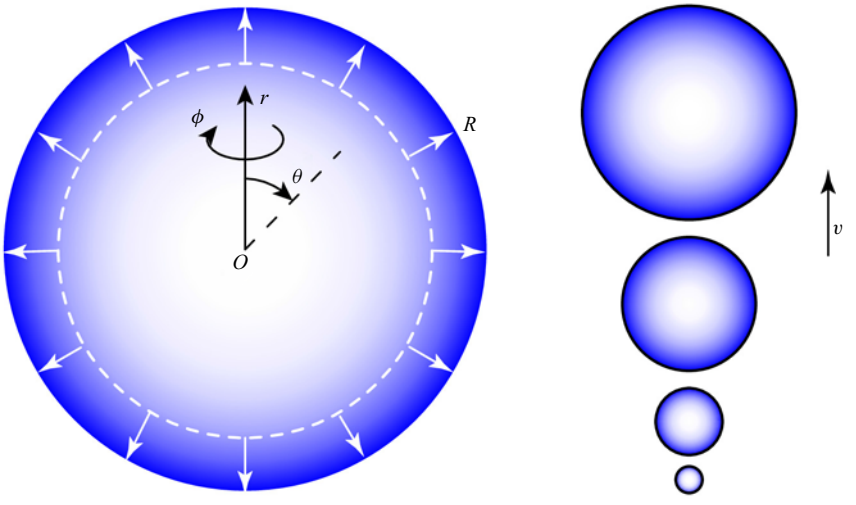


Figure 1. The definition of the axisymmetric model and coordinate system for bubble migration.

which is the fundamental governing differential equation for the velocity field. This scalar equation governs the spatial distribution of the combined kinetic energy terms under the influence of the potential flow advecting the vorticity.

In the dynamic modelling of a single bubble within fluid fields, Zhang *et al.* (2023, 2024) have invariably employed axisymmetric postulations. Consequently, when analysed through the spherical coordinate system $O-r\theta\phi$, the velocity field manifests dependencies solely upon spatial variables r and θ, while exhibiting no azimuthal (ϕ-direction) velocity component, as shown in figure 1. The velocity profiles within potential fields have been rigorously elucidated and mathematically prescribed:

$$u_{sr} = \frac{R^2\dot{R}}{r^2} + \frac{R^3 v}{r^3}\cos\theta, \tag{2.11a}$$

$$u_{s\theta} = \frac{R^3 v}{2r^3}\sin\theta, \tag{2.11b}$$

where R and v are the bubble radius and migration velocity, respectively, and u_{sr} and $u_{s\theta}$ represent the r- and θ-direction components of fluid velocity $\boldsymbol{u}_s$ of the potential field, respectively. Equations (2.11*a*) and (2.11*b*) describe the radial flow due to bubble oscillation and the dipole-like flow field induced by the translating bubble within an inviscid fluid. Upon expanding the left-hand side of (2.10) within the spherical coordinate framework, its scalar formulation through systematic resolution of the coordinate-specific differential operators and requisite tensor transformations is derived as

$$\begin{aligned}&\nabla\cdot\left[\nabla\left(\boldsymbol{u}_v\cdot\boldsymbol{u}_s+\frac{1}{2}u_v^2\right)+\boldsymbol{u}_s\cdot\nabla(\nabla\times\boldsymbol{u}_v)\right]\\&\quad=\nabla^2\left(u_{sr}u_{vr}+u_{s\theta}u_{v\theta}+\frac{1}{2}u_{vr}^2+\frac{1}{2}u_{v\theta}^2\right)+\nabla(\nabla\times\boldsymbol{u}_v):\nabla\boldsymbol{u}_s+\boldsymbol{u}_s\cdot\nabla^2(\nabla\times\boldsymbol{u}_v),\end{aligned} \tag{2.12}$$

https://doi.org/10.1017/jfm.2026.11252 Published online by Cambridge University Press

while for axisymmetric configurations, we find that $\boldsymbol{\nabla}(\boldsymbol{\nabla}\times\boldsymbol{u}_v):\boldsymbol{\nabla}\boldsymbol{u}_s=\boldsymbol{u}_s\cdot\nabla^2(\boldsymbol{\nabla}\times\boldsymbol{u}_v)=0$, which yields

$$\nabla^2\left(u_{sr}u_{vr}+u_{s\theta}u_{v\theta}+\frac{1}{2}u_{vr}^2+\frac{1}{2}u_{v\theta}^2\right)=0, \tag{2.13}$$

where u_{vr} and $u_{v\theta}$ represent the r- and θ-direction components of fluid velocity $\boldsymbol{u}_v$ of the viscous field in (2.12) and (2.13), respectively. Equation (2.13) is the Laplace equation governing a scalar quantity related to the energy of interaction between the potential and viscous flow fields. Its harmonic nature simplifies its solution.

Under the axisymmetric condition, the spherical coordinate manifestation of (2.13) unfolds with geometric grace:

$$\begin{aligned}&\frac{1}{r^2}\frac{\partial}{\partial r}\left[r^2\frac{\partial}{\partial r}\left(u_{sr}u_{vr}+u_{s\theta}u_{v\theta}+\frac{1}{2}u_{vr}^2+\frac{1}{2}u_{v\theta}^2\right)\right]\\&\quad+\frac{1}{r^2\sin\theta}\frac{\partial}{\partial\theta}\left[\sin\theta\,\frac{\partial}{\partial\theta}\left(u_{sr}u_{vr}+u_{s\theta}u_{v\theta}+\frac{1}{2}u_{vr}^2+\frac{1}{2}u_{v\theta}^2\right)\right]=0.\end{aligned} \tag{2.14}$$

Similarly, the fluid incompressibility condition expressed by (2.7) can be rigorously formulated in spherical coordinates as

$$\frac{1}{r^2}\frac{\partial}{\partial r}\left(r^2u_{vr}\right)+\frac{1}{r^2\sin\theta}\frac{\partial}{\partial\theta}\left(\sin\theta\,u_{v\theta}\right)=0. \tag{2.15}$$

This is the standard form of the continuity equation in spherical coordinates, ensuring no net mass flux through any infinitesimal volume. By simultaneously solving the coupled system (2.14)–(2.15), the desired solution can be elegantly derived as

$$u_{vr}=U_r-2u_{sr}, \tag{2.16a}$$

$$u_{v\theta}=U_\theta-2u_{s\theta}, \tag{2.16b}$$

where U_r and U_θ satisfy

$$\nabla^2\left(U_r^2-2U_ru_{sr}+U_\theta^2-2U_\theta u_{s\theta}\right)=0. \tag{2.17}$$

Indeed, the solution for the two unknowns, i.e. radial and tangential velocities, necessitates the simultaneous resolution of (2.17) and the incompressibility condition, followed by the application of boundary conditions to determine the unique solution to the differential equation. This essentially entails solving a system of binary quadratic second-order differential equations, a process that proves considerably arduous and intricate in theoretical computation. Given that the current theoretical model is established under viscous fluid conditions, the influence of bubble flow separation is physically negligible. Consequently, to facilitate tractable solutions, the model presupposes an absence of flow separation, which means that the circumfluent flow contributes negligibly to radial velocity. During equation resolution, strict adherence to (2.17) is rigorously enforced, though this deliberately compromises the rigorous fulfilment of the incompressibility condition at the fluid-element level. Considering the inherent orthogonality between U_r and U_θ, (2.17) may be reformulated in a more comprehensive manner as

$$(U_r-u_{sr})^2=u_{sr}^2+B_r, \tag{2.18a}$$

$$(U_\theta-u_{s\theta})=u_{s\theta}^2+B_\theta, \tag{2.18b}$$

https://doi.org/10.1017/jfm.2026.11252 Published online by Cambridge University Press

where both B_r and B_θ are harmonic functions satisfying $\nabla^2 B_r = \nabla^2 B_\theta = 0$. Equations (2.18*a*) and (2.18*b*) suggest that the deviation of the auxiliary variables U_r, U_θ from the potential field components is related to the potential flow energy itself plus a harmonic correction term. As viscous forces play a significant and dominant role, the viscous domain can be regarded as infinite. Based on the Navier slip condition and the continuity of shear stress, the bubble surface can be considered impermeable in the normal direction, and slip-free in the tangential direction, in theoretical treatments. This corresponds to the Stokes hypothesis, where the bubble size and migration velocity are negligible, typically applicable to microbubbles, i.e. cavitation bubbles during their expansion phase. If u_r and u_θ are regarded as the r- and θ-direction components of fluid velocity, respectively, then we have $u_{sr} = \dot{R} + v\cos\theta$ and $u_{s\theta} = v\sin\theta/2$ at the bubble surface, while $u_r = u_{sr} + u_{vr} = U_r - u_{sr} = \dot{R} + v\cos\theta$ and $u_\theta = u_{s\theta} + u_{v\theta} = U_\theta - u_{s\theta} = v\sin\theta$, yielding $B_r = 0$ and $B_\theta = 3v^2\sin^2\theta/4$. Meanwhile, we have $u_r = U_r - u_{sr} = u_{sr} = 0$ and $u_\theta = U_\theta - u_{s\theta} = u_{s\theta} = 0$ at infinity, resulting in $B_r = 0$ and $B_\theta = 0$. Leveraging these boundary conditions for B_r and B_θ, along with axisymmetry and periodicity constraints, we proceed to solve the governing equation $\nabla^2 B_r = \nabla^2 B_\theta = 0$, to obtain

$$B_r = 0, \tag{2.19a}$$

$$B_\theta = \left[\frac{R}{2r}\left(1 - \frac{R^2}{r^2}\right) + \frac{3R^3}{4r^3}\sin^2\theta\right] v^2. \tag{2.19b}$$

The harmonic function B_θ decays with distance from the bubble and varies with polar angle, representing the adjustment to the viscous field required to meet the boundary conditions. Substituting (2.19*a*) and (2.19*b*) into (2.18*a*) and (2.18*b*), respectively, the resultant solution is derived as

$$U_r = 2u_{sr}, \tag{2.20a}$$

$$U_\theta = u_{s\theta} + \sqrt{u_{s\theta}^2 + \left[\frac{R}{2r}\left(1 - \frac{R^2}{r^2}\right) + \frac{3R^3}{4r^3}\sin^2\theta\right] v^2}. \tag{2.20b}$$

Evidently, viscous effect remains inconsequential to the fluid velocity along the radial (r) dimension, whereas in the polar angular direction (θ) it manifests discernible influence:

$$u_{v\theta} = U_\theta - 2u_{s\theta} = v\left[\sqrt{\frac{R}{2r}\left(1 - \frac{R^2}{r^2}\right) + \left(\frac{3}{4} + \frac{R^3}{4r^3}\right)\frac{R^3}{r^3}\sin^2\theta} - \frac{R^3\sin\theta}{2r^3}\right], \tag{2.21}$$

which corresponds to the velocity field $\boldsymbol{u}_v = u_{v\theta}\boldsymbol{e_\theta}$ of a bubble under the description of polar coordinates. The final expression for the viscous tangential velocity component shows its dependence on radial distance, polar angle, bubble size and migration speed. It represents the deviation from the potential field solution due to viscous stresses.

Further, we solve the pressure of the viscous field. According to (2.4) without the unsteady term, the pressure distribution within the viscous field satisfies

$$\nabla p_v = \mu\nabla^2(\boldsymbol{u}_s + \boldsymbol{u}_v) - \rho\left(\boldsymbol{u}_v\cdot\nabla\boldsymbol{u}_s + \boldsymbol{u}_s\cdot\nabla\boldsymbol{u}_v + \boldsymbol{u}_v\cdot\nabla\boldsymbol{u}_v\right), \tag{2.22}$$

which indicates that the viscous pressure gradient is required to balance the viscous stress term and the nonlinear inertial terms associated with the viscous velocity field. Given that $\boldsymbol{u}_s = \nabla\varphi$, where φ is the velocity potential of the irrotational fluid, and under the incompressibility condition wherein the velocity potential satisfies the Laplace equation

https://doi.org/10.1017/jfm.2026.11252 Published online by Cambridge University Press

$\nabla^2\varphi = 0$, we derive (2.22) through the application of tensor calculus:

$$\begin{aligned}\nabla p_v &= \mu\nabla^2\boldsymbol{u}_v - \rho\left[(\boldsymbol{u}_v\cdot\nabla)\nabla\varphi + \nabla\varphi\cdot\nabla\boldsymbol{u}_v + \boldsymbol{u}_v\cdot\nabla\boldsymbol{u}_v\right]\\ &= \mu\nabla\times(\nabla\times\boldsymbol{u}_v) - \rho\left[(\boldsymbol{u}_v\cdot\nabla)\nabla\varphi + \nabla\varphi\cdot\nabla\boldsymbol{u}_v + \boldsymbol{u}_v\cdot\nabla\boldsymbol{u}_v\right],\end{aligned} \tag{2.23}$$

where $\boldsymbol{u}_v$ refers to (2.21). The reformulation uses a vector identity for the Laplacian, and expresses the pressure gradient in terms of the vorticity of the viscous field and the convective acceleration terms. Expressing (2.23) in polar coordinates, the scalar form in the radial (r) and angular (θ) directions is derived as, respectively,

$$\frac{\partial p_v}{\partial r} = \frac{\mu v}{r\sin\theta}\frac{\partial^2(Qr\sin\theta)}{r\,\partial r\,\partial\theta} - \frac{\rho v^2}{2}\left[\frac{\partial Q^2}{\partial r} + \frac{\partial}{\partial r}\left(\frac{QR^3\sin\theta}{r^3}\right)\right], \tag{2.24a}$$

$$\frac{\partial p_v}{r\,\partial\theta} = -\frac{\mu v}{r\sin\theta}\frac{\partial^2(Qr\sin\theta)}{\partial r^2} - \frac{\rho v^2}{2}\left[\frac{\partial Q^2}{r\,\partial\theta} + \frac{\partial}{r\,\partial\theta}\left(\frac{QR^3\sin\theta}{r^3}\right)\right], \tag{2.24b}$$

where Q is

$$Q = \sqrt{\frac{R}{2r}\left(1-\frac{R^2}{r^2}\right) + \left(\frac{3}{4}+\frac{R^3}{4r^3}\right)\frac{R^3}{r^3}\sin^2\theta} - \frac{R^3\sin\theta}{2r^3}, \tag{2.25}$$

which represents the non-dimensionalised viscous tangential velocity component $u_{v\theta}/v$, simplifying the notation in the pressure equations. Let the pressure component corresponding to the μ term be denoted as $p_{v\mu}$, such that

$$\frac{\partial p_{v\mu}}{\partial r} = \frac{\mu v}{r\sin\theta}\frac{\partial^2(Qr\sin\theta)}{r\,\partial r\,\partial\theta}, \tag{2.26a}$$

$$\frac{\partial p_{v\mu}}{r\,\partial\theta} = -\frac{\mu v}{r\sin\theta}\frac{\partial^2(Qr\sin\theta)}{\partial r^2}, \tag{2.26b}$$

which define the part of the viscous pressure field $p_{v\mu}$ that arises solely from viscous stresses. By integrating (2.24*a*) and (2.24*b*), the pressure within the viscous field can be expressed in the form

$$p_v = p_{v\mu} - \frac{\rho v^2}{2}\left(Q^2 + \frac{QR^3\sin\theta}{r^3}\right) + p_a, \tag{2.27}$$

where p_a is the ambient pressure of the viscous field, which incorporates contributions from both the ambient hydrostatic pressure and the pressure of the potential field. Equation (2.27) is the pressure field of bubble in a viscous fluid under the description of polar coordinates. The total viscous pressure consists of a viscous stress contribution, a dynamic pressure term related to the kinetic energy of the viscous flow, and the ambient pressure.

2.2. *The drag force and coefficient for a spherical bubble*

Based on the Zhang equation (Zhang *et al.* 2024), if the fluid is static without boundaries, then the bubble oscillation and migration are characterised as

$$\left(\frac{C-\dot R}{R}+\frac{\mathrm{d}}{\mathrm{d}t}\right)\left\{\frac{R^2}{C}\left[\frac{1}{2}\left(\dot R-\frac{\dot m}{\rho}\right)^2+\frac{1}{4}v^2+H\right]\right\}+\frac{\mathrm{d}}{\mathrm{d}t}\left(R^2\frac{\dot m}{\rho}\right) = R^2\ddot R + 2R\dot R^2, \tag{2.28}$$

https://doi.org/10.1017/jfm.2026.11252 Published online by Cambridge University Press

$$\left[1-\frac{R\ddot{R}}{\left(C-\dot{R}\right)\dot{R}}+\frac{R}{C-\dot{R}}\frac{\mathrm{d}}{\mathrm{d}t}\right]\left(\frac{1}{2}R^3\dot{v}+\frac{3}{2}R^2\dot{R}v\right)$$
$$=\left[1-\frac{R\ddot{R}}{\left(C-\dot{R}\right)\dot{R}}+\frac{R}{C}\frac{\mathrm{d}}{\mathrm{d}t}\right]\left[\frac{\rho_g}{\rho}R^3\left(g-\dot{v}\right)-3R^2\frac{\dot{m}}{\rho}v+gR^3-\frac{3}{8}C_dR^2v^2\right], \tag{2.29}$$

where C is the sound speed, g is the gravity acceleration, ρ_g is the density of the bubble, C_d is the drag coefficient, H is the enthalpy difference between bubble and infinity, $\dot{m}$ is the mass transfer rate of per unit area, $\dot{v}$ is the bubble migration acceleration, and $\dot{R}$ and $\ddot{R}$ are the bubble oscillation velocity and acceleration, respectively. It is obvious that the C_d term controls the viscous force on the bubble; to compute the shape-induced drag force experienced by bubble migration, the pressure within the viscous field is integrated over the bubble surface along the direction of migration:

$$\oint_{S_b}p_v\boldsymbol{n}\cdot\boldsymbol{e}_z\,\mathrm{d}S=\oint_{S_b}p_{v\mu}\boldsymbol{n}\cdot\boldsymbol{e}_z\mathrm{d}S-\oint_{S_b}\frac{3}{8}\rho v^2\sin^2\theta\cos\theta\,\mathrm{d}S=\oint_{S_b}p_{v\mu}\boldsymbol{n}\cdot\boldsymbol{e}_z\,\mathrm{d}S, \tag{2.30}$$

where $\boldsymbol{n}$ denotes the unit normal vector to the bubble surface S_b, and $\boldsymbol{e}_z$ represents the basis vector aligned with the direction of migration. The total viscous pressure consists of a viscous stress contribution, a dynamic pressure term related to the kinetic energy of the viscous fluid, and the ambient pressure. For the unbounded field, one may employ the inverse application of the divergence theorem to further refine (2.30) as

$$\begin{aligned}
&\oint_{S_b}p_{v\mu}\boldsymbol{n}\cdot\boldsymbol{e}_z\,\mathrm{d}S=\int_V\nabla p_{v\mu}\cdot\boldsymbol{e}_z\mathrm{d}V=\int_V\left(\frac{\partial p_{v\mu}}{\partial r}\cos\theta-\frac{\partial p_{v\mu}}{r\,\partial\theta}\sin\theta\right)\mathrm{d}V\\
&=2\pi\mu Rv\int_0^{\pi}\int_r^R\left[\cos\theta\frac{\partial^2\left(Qr\sin\theta\right)}{\partial r\,\partial\theta}+r\sin\theta\frac{\partial^2\left(Qr\sin\theta\right)}{\partial r^2}\right]\mathrm{d}r\,\mathrm{d}\theta\\
&=2\pi\mu Rv\int_0^{\pi}\int_r^R\frac{\partial}{\partial r}\left[r\cos\theta\frac{\partial^2\left(Qr\sin\theta\right)}{\partial r\,\partial\theta}\right]\mathrm{d}r\,\mathrm{d}\theta\\
&-2\pi\mu Rv\int_0^{\pi}\int_r^R\frac{\partial}{r\,\partial\theta}\left[r\cos\theta\frac{\partial^2\left(Qr\sin\theta\right)}{\partial r^2}\right]\mathrm{d}r\mathrm{d}\theta\\
&=2\pi\mu Rv\left\{\int_0^{\pi}\left[r\sin^2\theta\left(r\frac{\partial Q}{\partial r}+Q\right)\right]_r^R\mathrm{d}\theta-\int_r^R\left[\left(r\frac{\partial Q}{\partial r}+Q\right)\sin\theta\cos\theta\right]_0^{\pi}\mathrm{d}r\right\}\\
&=\frac{37}{3}\pi\mu Rv-\frac{8\pi\mu R^3v}{3r^2}\\
&-\frac{4\pi\mu rv}{\sqrt{\frac{R}{2r}\left(1-\frac{R^2}{r^2}\right)+\left(\frac{3}{4}+\frac{R^3}{4r^3}\right)\frac{R^3}{r^3}}}\left[\frac{R}{4r}\left(1+\frac{R^2}{r^2}\right)+\frac{\left(\frac{15R}{8r}+\frac{R^4}{r^4}\right)\left(2+\frac{R^2}{r^2}+\frac{R^5}{r^5}\right)}{3+\frac{R^3}{r^3}}\right]E(n)\\
&+\frac{4\pi\mu rv}{\sqrt{\frac{R}{2r}\left(1-\frac{R^2}{r^2}\right)+\left(\frac{3}{4}+\frac{R^3}{4r^3}\right)\frac{R^3}{r^3}}}\left[\frac{R}{4r}\left(1+\frac{R^2}{r^2}\right)+\frac{\left(\frac{15R}{4r}+\frac{2R^4}{r^4}\right)\left(1-\frac{R^2}{r^2}\right)}{3+\frac{R^3}{r^3}}\right]K(n),
\end{aligned} \tag{2.31}$$

https://doi.org/10.1017/jfm.2026.11252 Published online by Cambridge University Press

where V denotes the fluid volume of the integral field from r to R, with r decided by the practical theoretical model whether finite or not, which is related to the Reynolds number. Here, $K(n)$ and $E(n)$ denote the complete elliptic integrals of the first and second kind, respectively, where n represents the modulus of the elliptic integral that satisfies

$$n=\sqrt{\frac{\left(\frac{3}{4}+\frac{R^3}{4r^3}\right)\frac{R^3}{r^3}}{\frac{R}{2r}\left(1-\frac{R^2}{r^2}\right)+\left(\frac{3}{4}+\frac{R^3}{4r^3}\right)\frac{R^3}{r^3}}}, \tag{2.32}$$

which yields the force on the bubble due to the viscous pressure $p_{v\mu}$, expressed in elliptic integrals that arise from the specific form of the velocity field Q. If we set $r=kR$ $(1<k\leq\infty)$, meaning that the outer surface of the integral field is k times the bubble radius R, then rewrite (2.31) and (2.32) as

$$\begin{aligned}\oint_{S_b} p_{v\mu}\boldsymbol{n}\cdot\boldsymbol{e}_z\,\mathrm{d}S&=\left(\frac{37}{3}-\frac{8}{3k^2}\right)\pi\mu Rv+\frac{2k\left(1+k^2\right)}{\sqrt{1+k^3+2k^5}}\left[K(n)-E(n)\right]\pi\mu Rv\\&+\frac{8+15k^3}{k^2\left(1+3k^3\right)\sqrt{1+k^3+2k^5}}\left[2k^3\left(k^2-1\right)K(n)-\left(1+k^3+2k^5\right)E(n)\right]\pi\mu Rv,\end{aligned} \tag{2.33}$$

where

$$n=\sqrt{\frac{1+3k^3}{1+k^3+2k^5}}, \tag{2.34}$$

then (2.33) and (2.34) express the pressure drag force in terms of the dimensionless parameter k, which defines the outer limit of the integration domain relative to the bubble radius. Building upon this foundation, it is imperative to incorporate the frictional resistance, thereby enabling the derivation of viscous drag resistance acting on the bubble:

$$\begin{aligned}D&=\oint_{S_b}\left(p_v\boldsymbol{n}\cdot\boldsymbol{e}_z-\sigma_{rr}\boldsymbol{n}\cdot\boldsymbol{e}_z+\sigma_{r\theta}\boldsymbol{\tau}\cdot\boldsymbol{e}_z\right)\,\mathrm{d}S\\&=\oint_{S_b}\left[p_{v\mu}\boldsymbol{n}\cdot\boldsymbol{e}_z-2\mu\frac{\partial u_r}{\partial r}+\mu\left(\frac{\partial u_r}{r\,\partial\theta}+\frac{\partial u_\theta}{\partial r}-\frac{u_\theta}{r}\right)\right]\mathrm{d}S\\&=\left(12-\frac{8}{3k^2}\right)\pi\mu Rv+\frac{2k\left(1+k^2\right)}{\sqrt{1+k^3+2k^5}}\left[K(n)-E(n)\right]\pi\mu Rv\\&+\frac{8+15k^3}{k^2\left(1+3k^3\right)\sqrt{1+k^3+2k^5}}\left[2k^3\left(k^2-1\right)K(n)-\left(1+k^3+2k^5\right)E(n)\right]\pi\mu Rv,\end{aligned} \tag{2.35}$$

where $\boldsymbol{\tau}$ denotes the unit tangential vector to the bubble surface, and σ_{rr} and $\sigma_{r\theta}$ denote the magnitudes of the normal and tangential frictional stresses acting on the bubble surface, respectively. The total drag force D includes contributions from the viscous pressure $(p_{v\mu}\boldsymbol{n}\cdot\boldsymbol{e}_z)$, the normal viscous stress $(-\sigma_{rr}\boldsymbol{n}\cdot\boldsymbol{e}_z)$, and the tangential viscous stress $(\sigma_{r\theta}\boldsymbol{\tau}\cdot\boldsymbol{e}_z)$. By introducing the Reynolds number for bubble migration as $Re=2\rho Rv/\mu$ and defining the drag coefficient $C_d=D/(\rho\pi R^2v^2/2)$, the functional dependence between the Reynolds number and the drag coefficient can be systematically

https://doi.org/10.1017/jfm.2026.11252 Published online by Cambridge University Press

established:

$$C_d = \frac{48}{Re}\left\{1 - \frac{2}{9k^2} + \frac{k\left(1+k^2\right)\left[K(n) - E(n)\right]}{6\sqrt{1+k^3+2k^5}} + \frac{\left(8+15k^3\right)\left[2k^3\left(k^2-1\right)K(n) - \left(1+k^3+2k^5\right)E(n)\right]}{12k^2\left(1+3k^3\right)\sqrt{1+k^3+2k^5}}\right\}. \tag{2.36}$$

This is the central result for the drag coefficient, showing its dependence on Reynolds number Re and the integration domain parameter k. The term $48/Re$ is the classic low-Re result, and the terms in the bracket represent corrections due to the finite domain size k and the specific velocity profile. When a bubble resides within an infinite viscous field, corresponding to the asymptotic limit $r \to \infty$ (and equivalently $k \to \infty$), the drag coefficient C_d reduces to

$$C_d = \frac{48}{Re}. \tag{2.37}$$

This represents the scaling law associated with low-Reynolds-number hydrodynamics ($Re \leq 1$), where (2.37) exhibits structural congruence with both the analytical derivations from Levich (1962) and Moore (1963), and the classical Stokes solution (the tangential velocity surrounding bubble should be replaced by $v \sin\theta/2$, as displayed in Appendix A). In the limit of an infinite domain ($k \to \infty$), the complex corrections vanish, recovering the well-known theoretical result for drag on a spherical bubble.

However, when bubbles enter the collapse phase accompanied by rapid migration, the corresponding transient Reynolds number significantly exceeds 1. Under such conditions, the bubble surface transitions from a no-slip boundary condition to an idealised free-slip condition, where tangential stress vanishes entirely. Assuming negligible fluid impurities and chemical interactions, this state aligns fundamentally with the premises of potential flow theory. Notably, while frictional resistance disappears, this does not imply drag-free motion. High-speed flow around the bubble induces pronounced flow separation, generating substantial form drag that severely restricts bubble migration. This constitutes the most critical distinction from potential flow predictions. Regrettably, the velocity and pressure fields post-flow-separation prove prohibitively complex for analytical derivation, as no quantitative framework currently exists to characterise these parameters. However, we note a potentially significant observation: analysis by Moore (1963), though predicated on $Re \geq 1$, also yielded $C_d = 48/Re$. This counterintuitively suggests that form drag induced by flow separation at high Reynolds numbers may exhibit comparable magnitude to the form drag under no-slip, no-separation conditions. Building upon this hypothesis, we may potentially establish a novel theoretical framework capable of continuously bridging diverse Reynolds number regimes.

It is evident that as the Reynolds number (Re) increases, inertial forces progressively supplant viscous forces as the dominant factor, thereby prompting the transition of the integration domain from an infinite expanse to a finite boundary layer. Within this context, the Reynolds number governs the corresponding boundary layer thickness, necessitating a more in-depth analysis of the interdependence between boundary layer thickness $\delta = r - R = (k-1)R$ and Re. The parameter k (and thus the integration limit r) is not arbitrary but is physically determined by the thickness of the region where viscous effects are significant, i.e. the boundary layer. Derived from the boundary conditions of the velocity field $u_{v\theta}(r = R) = 3v\sin\theta/2$ and $u_{v\theta}(r = \delta + R) = 0$, given that the

https://doi.org/10.1017/jfm.2026.11252 Published online by Cambridge University Press

asymptotic vanishing condition of (2.21) at infinity cannot be rigorously enforced via coordinate substitution at $r = \delta + R$, a polynomial fitting methodology is employed herein to reconstruct the viscous velocity field within the boundary layer interior. If the viscous velocity distribution within the boundary layer is represented in the spherical coordinate system as $\boldsymbol{u}_v = (0,\ u_{v\delta},\ 0)$, where the radial and azimuthal components vanish while the polar angular component $u_{v\delta}$ characterises the tangential motion, then

$$u_{v\delta} = \frac{3}{2} v \sin\theta \left(a_0 + a_1\eta + a_2\eta^2\right), \tag{2.38}$$

where $\eta = (\delta + R - r)/\delta$; as the boundary layer thickness constitutes a negligible quantity relative to the bubble scale, (2.38) retains approximation fidelity solely through quadratic terms in its polynomial expansion. The velocity profile must exhibit smoothness at the bubble surface, requiring $\mathrm{d}u_{v\delta}/\mathrm{d}\eta = 0$ at $r = R$. Integrating this condition with velocity boundary conditions, one derives $a_0 = 0$, $a_1 = 2$, $a_2 = -1$. Then (2.38) can be rewritten as

$$u_{v\delta} = \frac{3}{2} v \sin\theta \left(2\eta - \eta^2\right). \tag{2.39}$$

Consequently, the momentum deficit thickness of the boundary layer is formulated as

$$\vartheta = \int_R^{\delta+R} \frac{u_{v\delta}}{u_{v\theta}\ (r=R)} \left[1 - \frac{u_{v\delta}}{u_{v\theta}\ (r=R)}\right] \mathrm{d}r = \frac{2\delta}{15}, \tag{2.40}$$

along with the displacement thickness of the boundary layer

$$\delta^* = \int_R^{\delta+R} \left[1 - \frac{u_{v\delta}}{u_{v\theta}\ (r=R)}\right] \mathrm{d}r = \frac{\delta}{3}. \tag{2.41}$$

Based on the von Kármán momentum integral equation with $u_{v\delta}(r = R) = 3v\sin\theta/2$ as

$$\frac{1}{R}\frac{\mathrm{d}}{\mathrm{d}\theta}\left(\frac{9\vartheta}{4} v^2 \sin^2\theta\right) + \frac{9\delta^*}{4R} v^2 \sin\theta\cos\theta = \frac{\sigma_{r\theta}}{\rho}, \tag{2.42}$$

substituting (2.40) and (2.41) into (2.42) yields

$$2\sin\theta\,\delta\frac{\mathrm{d}\delta}{\mathrm{d}\theta} + 9\cos\theta\,\delta^2 = \frac{20\mu R}{\rho v}. \tag{2.43}$$

Then solving (2.43) yields the boundary layer thickness as

$$\frac{\delta}{R} = \sqrt{\frac{40}{Re\sin^9\theta}\left(\frac{35\theta}{128} - \frac{7}{32}\sin 2\theta + \frac{7}{128}\sin 4\theta - \frac{\sin 6\theta}{96} + \frac{\sin 8\theta}{1024}\right)}, \tag{2.44}$$

and k satisfies

$$k = 1 + \sqrt{\frac{40}{Re\sin^9\theta}\left(\frac{35\theta}{128} - \frac{7}{32}\sin 2\theta + \frac{7}{128}\sin 4\theta - \frac{\sin 6\theta}{96} + \frac{\sin 8\theta}{1024}\right)}. \tag{2.45}$$

Noting that k exhibits angular dependence on θ, we adopt the value corresponding to the upstream-facing equatorial cross-section of the spherical bubble as the representative parameter value for computational expediency, where $k = k(\pi/2) = 1 + 4.14/\sqrt{Re}$.

2.3. *The modification for bubble collapse deformation*

Notably, with respect to the drag coefficient governing bubble migration, Li *et al.* (2014) elucidated that elevated bubble migration velocities induce compressive deformation of

https://doi.org/10.1017/jfm.2026.11252 Published online by Cambridge University Press

the upstream-facing dimension, prompting a morphological transition from spherical to ellipsoidal configurations. This geometric alteration consequently precipitates a marked elevation (Loth 2008) in the drag coefficient. Nevertheless, while the theoretical framework developed herein fundamentally assumes spherical bubble morphology, pragmatic adaptations have been implemented through the introduction of an ellipsoidal deformation factor to modify select governing equations. Though this methodology compromises mathematical rigour in addressing ellipsoidal bubble dynamics, it yields solutions characterised by enhanced operational tractability, analytical conciseness, and deviations constrained within acceptable tolerance thresholds.

By postulating an ellipsoidal bubble configuration with semi-major axis a and semi-minor axis b, while maintaining invariant total bubble volume, a functional correspondence may be established between the spherical equivalent radius R and the principal axes dimensions (a, b) through volumetric conservation principles as $R^3 = a^2 b$. By defining the geometric coefficient as the aspect ratio of the ellipsoid $a/b = \epsilon \geq 1$, the spherical equivalent radius is derived as $R = a/\sqrt[3]{\epsilon}$. Consequently, the Reynolds number for the ellisopidal configuration necessitates scaling the spherical Re by a factor $1/\sqrt[3]{\epsilon}$ to account for geometric anisotropy. To account for variations in frontal projected area, viscous drag is thereby modified through the introduction of a geometric correction function. The function $\Gamma(\epsilon)$ is based on the surface area of an axisymmetric oblate spheroid relative to that of a sphere of equivalent volume; it provides a scaling factor for the drag increase due to the enlarged wetted surface area of the deformed bubble:

$$\Gamma(\epsilon) = \frac{\epsilon^{2/3}}{2}\left[1 + \frac{\ln\left(\epsilon + \sqrt{\epsilon^2 - 1}\right) - \ln\left(\epsilon - \sqrt{\epsilon^2 - 1}\right)}{2\epsilon\sqrt{\epsilon^2 - 1}}\right]. \tag{2.46}$$

Consequently, the drag coefficient for the deformed bubble configuration can be expressed based on (2.36) as

$$C_d = \frac{48}{Re}\Gamma(\epsilon)\sqrt[3]{\epsilon}\left\{1 - \frac{2}{9k^2} + \frac{k\left(1+k^2\right)\left[K(n) - E(n)\right]}{6\sqrt{1+k^3+2k^5}} + \frac{\left(8+15k^3\right)\left[2k^3\left(k^2-1\right)K(n) - \left(1+k^3+2k^5\right)E(n)\right]}{12k^2\left(1+3k^3\right)\sqrt{1+k^3+2k^5}}\right\}. \tag{2.47}$$

Experimental determination of ϵ provides empirical validation for this framework. Furthermore, while the closed-form analytical expressions derived herein maintain precision under prescribed conditions, the bubble collapse process inherently involves jet formation that drastically compresses the minor axis (Lee *et al.* 2011; Zhang *et al.* 2001; Wang *et al.* 2022). Progressive adjustment of ϵ from 1 becomes warranted once Re exceeds 500–600, with the geometric coefficient reaching a critical threshold of the order of $O(10^4)$ during the jet penetration event.

In summary, the viscous drag coefficient C_d governing bubble migration can be determined via (2.47), where the modulus n of the elliptic integral is derived from (2.34), and the integration domain coefficient k adopts the typical value prescribed by (2.45) based on the instantaneous bubble migration Reynolds number. Since the Reynolds number evolves dynamically throughout the migration process, the drag coefficient C_d correspondingly exhibits temporal variation (Yan *et al.* 2017). This time-dependent C_d is iteratively incorporated into the transient bubble migration equation (2.29), thereby

https://doi.org/10.1017/jfm.2026.11252 Published online by Cambridge University Press

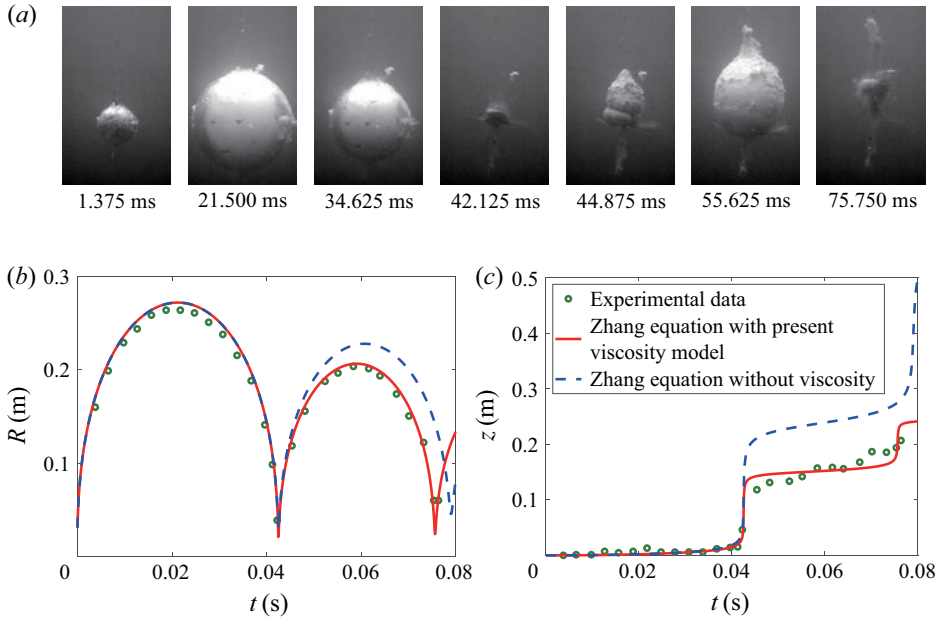


Figure 2. Underwater explosive bubble experiment and comparisons between theoretical and experimental results in a gravity field. (*a*) Selected sequential high-speed images of the underwater explosive bubble. (*b*) Comparison of the bubble oscillation radius. (*c*) Comparison of the bubble migration displacement. Green dots indicate experimental data, the red solid line is given by this model (see § 2), and the blue dashed line is given by the Zhang equation without viscosity ($C_d = 0$).

enabling real-time updates to both migration velocity and positional coordinates through numerical resolution.

3. Results analysis

3.1. *Comparison and description of results*

In characterising the dynamic behaviour of spherical bubbles within viscous fluids, we have benchmarked our theoretical framework against the experimental data. The experiment is conducted within an $8 \times 8 \times 8$ m^3 water tank, employing methodologies for both experimentation and filming that are derived from previous work (Liu *et al.* 2021; Zhang *et al.* 2023). The pertinent experimental parameters are enumerated as follows: a bubble generated by a 4 g Hexogen explosive at water depth 4 m, with surrounding fluid density 1000 kg m^{-3}, surface tension coefficient 0.075 N m^{-1}, and dynamic viscosity coefficient 1×10^{-3} Pa s. The high-speed images of the bubble are shown in figure 2(*a*). Numerical predictions from our proposed model undergo rigorous validation through comparative analysis with experimental data, with inviscid fluid assumption cases incorporated for benchmarking. The temporal evolutions of bubble oscillation radius and migration displacement across these scenarios are graphically illustrated in figures 2(*b*) and 2(*c*), respectively.

As illustrated in figure 2(*b*), the oscillation characteristics of bubbles remain fundamentally unaltered irrespective of whether fluid viscosity is considered during the first period. This conclusion is unequivocally validated by the striking congruence between these distinct computational implementations of the Zhang equation, where observed minute discrepancies in localised regions stem solely from iterative precision limitations

https://doi.org/10.1017/jfm.2026.11252 Published online by Cambridge University Press

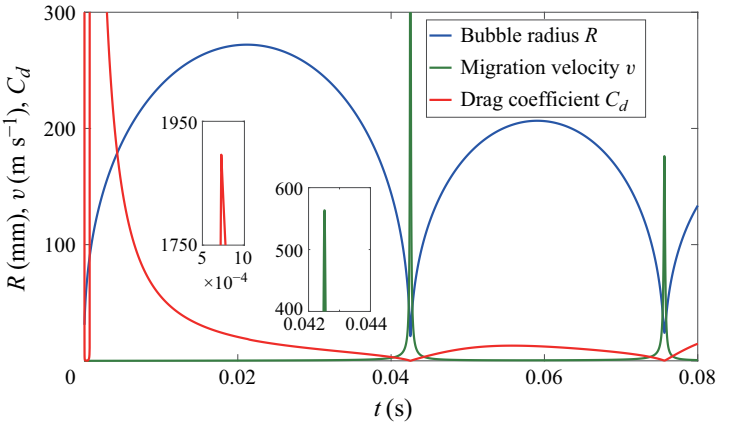


Figure 3. Bubble oscillation radius R, migration velocity v and drag coefficient C_d by the theoretical model under experimental conditions (a 4 g Hexogen explosive bubble, water depth 4 m, fluid density 1000 kg m^{-3}, surface tension coefficient 0.075 N m^{-1} and dynamic viscosity coefficient 1×10^{-3} Pa s).

in numerical calculations. Such findings provide additional empirical confirmation of the seminal proposition regarding the negligible hydrodynamic role of fluid viscosity in bubble oscillation by Yang & Yeh (1966). Meanwhile, the theoretical model proposed in this study exhibits a superior degree of congruence with experimental results, demonstrating that the Zhang equation achieves enhanced precision not only in predicting bubble oscillation characteristics, but also in describing bubble migration patterns. The Reynolds number for bubble migration is predominantly below $O(10^4)$ during most of the oscillation period. To provide a more intuitive representation of the temporal variations in bubble radius, migration velocity and drag coefficient under the aforementioned conditions, these interdependent parameters are comprehensively visualised through their concurrent presentation in figure 3.

As shown in figure 3, both the bubble radius and migration velocity vary over time. Consequently, the drag coefficient C_d also changes dynamically. Initially, when the bubble is in its excited state, its radius and velocity are very small. At this stage, the Reynolds number is also low, resulting in a significantly large drag coefficient, with a peak value approaching 1900. However, this large C_d value does not necessarily imply a correspondingly large drag force at that time. As the bubble expands, although its migration velocity shows no significant change, the rapid increase in bubble radius leads to a rise in the Reynolds number. This, in turn, causes the drag coefficient C_d to decrease rapidly. Importantly, the moment of maximum bubble volume does not correspond to an extremum in C_d. This is because the decrease in parameter k in (2.47) causes C_d to maintain its downward trend. In contrast, the extremum of C_d within a cycle actually appears during the bubble's expansion phase. As the bubble enters the collapse phase, the parameter k increases with the decrease in the Reynolds number. This causes the exponent n to gradually shift from 1 towards 0. Considering the mathematical properties of the elliptic integrals $K(n)$ and $E(n)$, their contribution diminishes. However, because the oscillation rate during collapse transitions from gradual to rapid change, the reduction in the contribution from the elliptic integral term becomes the dominant effect. During the collapse to the minimum bubble size, significant migration occurs, with velocities reaching hundreds of metres per second. In subsequent cycles, the peak migration velocity progressively attenuates due to energy dissipation caused by fluid viscosity and compressibility (Wang 2016). At this minimum size point, the Reynolds number Re

https://doi.org/10.1017/jfm.2026.11252 Published online by Cambridge University Press

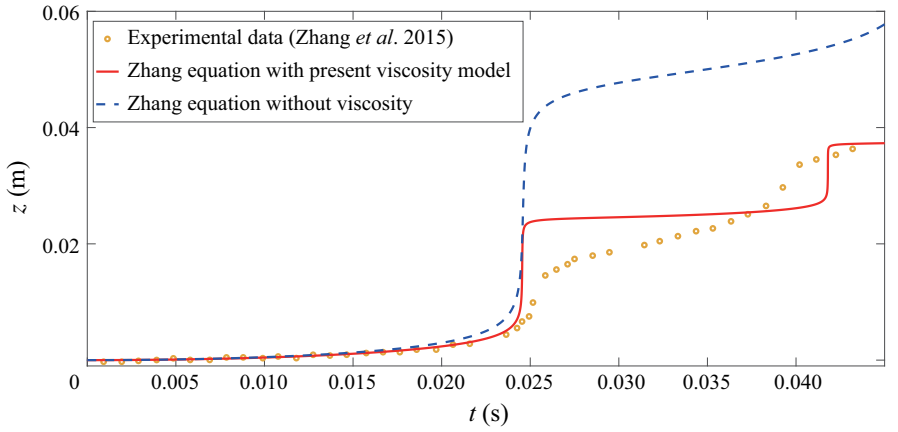


Figure 4. The bubble migration displacement. Yellow dots indicate experimental data from Zhang *et al.* (2015), the red solid line is given by this model (see § 2), and the blue dashed line is given by the Zhang equation without viscosity ($C_d = 0$).

increases rapidly. Concurrently, the actual jet induces significant bubble deformation. Although C_d decreases to a very low value, the oblate spheroid correction function in (2.46) suppresses the tendency of C_d to approach zero, thereby ensuring the continued effect of viscous forces.

Furthermore, another comparative analysis was performed using the experimental data from Zhang *et al.* (2015), specifically selecting cases with buoyancy parameter 0.211 for the bubble in a free field where the ambient pressure is 9.75 kPa, the maximum bubble radius can reach 32.4 mm, and the saturated vapour pressure is 2338 Pa. The migration displacement of the bubble is depicted in figure 4. A comparison of the results in figure 4 reveals that during the initial stage of bubble migration, the theoretical model exhibits good agreement with experimental data, where the lower Reynolds numbers above $O(10^3)$ also dominate most of the oscillation period. However, as the bubble enters rapid migration and transitions to subsequent cycles, its non-spherical deformation considerably complicates the fluid environment. While the model incorporates approximate modifications for large deformations in § 2.3, it is difficult to dynamically characterise the migration behaviour in later experimental cycles due to constraints imposed by inherent model assumptions and the precision of these modifications. While existing models cannot precisely characterise non-spherical migration beyond the initial cycles, the spherical model enables highly accurate prediction of migration amplitude during the first few bubble cycles. Similarly, we present the bubble radius, migration velocity and drag force curves derived from the theoretical model results in figure 4, as illustrated in figure 5. As indicated by the definition of drag force $D = \pi\rho C_d R^2 v^2/2$, the drag coefficient C_d increases sharply during the rapid migration of bubbles in the collapse phase. Despite the diminished bubble radius at this stage, the combined effect of the squared velocity and amplified drag coefficient results in an instantaneous surge of drag force that reaches its peak value.

We also referenced the experimental results of Hung & Hwangfu (2010) and Kong *et al.* (2019) on bubbles ascending in viscous fluids to validate the accuracy and efficiency of the analytical theoretical model. In Kong's study, the DNS methodology for numerical simulations was employed and compared to the results with experimental data (rising bubble for 60 wt glycerol at 1.1 ml min^{-1} gas flow rate). Under the conditions of density 1.153×10^3 kg m^{-3}, viscosity coefficient 1.08×10^{-2} Pa s, and surface tension coefficient 6.77×10^{-2} N m^{-1}, the bubble was released from the bottom of the tank.

https://doi.org/10.1017/jfm.2026.11252 Published online by Cambridge University Press

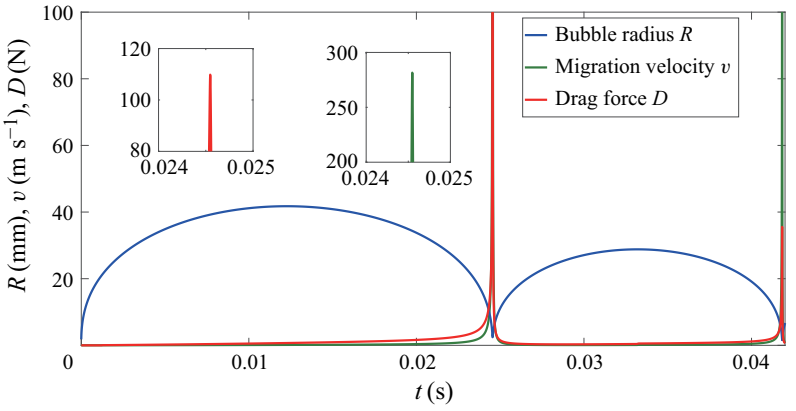


Figure 5. Bubble oscillation radius R, migration velocity v and drag force D by the theoretical model under Zhang *et al.* (2015) experimental conditions (ambient pressure 9.75 kPa, maximum bubble radius can reach 32.4 mm, and saturated vapour pressure 2338 kPa).

Experimental observations recorded maximum bubble diameter 3.11×10^{-3} m. Since the experimental bubble was generated at the bottom of the tank, it can be considered as isobaric and subject to the influence of the bottom boundary. Based on the theoretical model, we compared the bubble migration velocity against the experimentally observed curves both with and without accounting for viscous drag, as illustrated in figure 6. It is noteworthy that during the initial migration phase, the bubbles are significantly affected by the bottom boundary, which encompasses both non-spherical deformation and the effects of boundary conditions. As the bubble ascends, the attractive influence of the boundary conditions gradually diminishes. However, the relatively mild oscillation of the isobaric bubble does not substantially alter the aspect ratio ϵ of the non-spherical bubble. Nevertheless, due to the inherent limitations of the theoretical model's assumptions, which fail to incorporate the attractive effects of the boundary conditions, a discernible discrepancy arises in the early migration stage due to boundary influences. As the boundary effects weaken subsequently, and based on morphological observations from the reference, we set $\epsilon = 1.5$, resulting in excellent agreement between the theoretical predictions and experimental data. Apart from the initial boundary-induced discrepancies, the computational efficiency of the theoretical model is markedly superior to that of DNS or other numerical methods.

In Hung's study, the experimental conditions involved fluid density 1×10^3 kg m^{-3}, viscosity coefficient 1×10^{-3} Pa s, and surface tension coefficient 0.072 N m^{-1}. The bubble was set by an explosion of 1.12 g TNT with non-dimensional stand-off as 0.96–35 mm St plate boundary. The bubble was released at depth 2.55 m, and the migration displacement was measured as it ascended. Similar to Kong's experiment, we compared the bubble migration displacement against the experimentally observed curves both with and without accounting for viscous drag, as illustrated in figure 7. The theoretical model exhibits excellent agreement with the experimental data throughout the entire migration process. This further validates the accuracy and efficiency of the theoretical model proposed in this study for characterising bubble migration in viscous fluids.

3.2. *The variation pattern of the drag coefficient*

Regarding the drag coefficient C_d, which primarily depends on the instantaneous Reynolds number of the fluid, a systematic comparison between the C_d–Re relationship derived from

https://doi.org/10.1017/jfm.2026.11252 Published online by Cambridge University Press

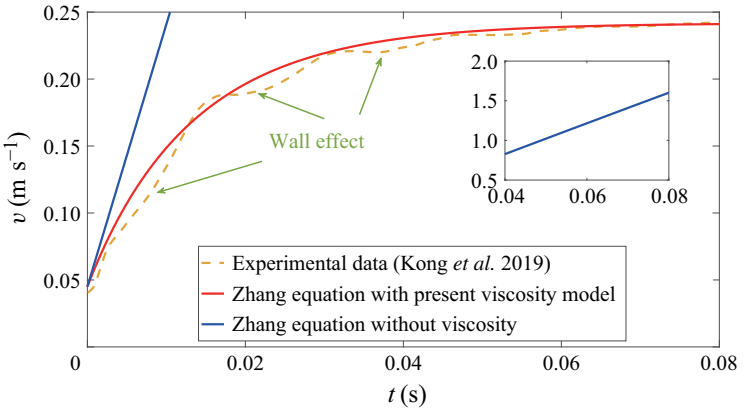


Figure 6. The bubble migration velocity. The yellow dashed line indicates the experimental data cited from Kong *et al.* (2019), the red solid line is given by this model (see § 2), and the blue solid line is given by the Zhang equation without viscosity ($C_d = 0$).

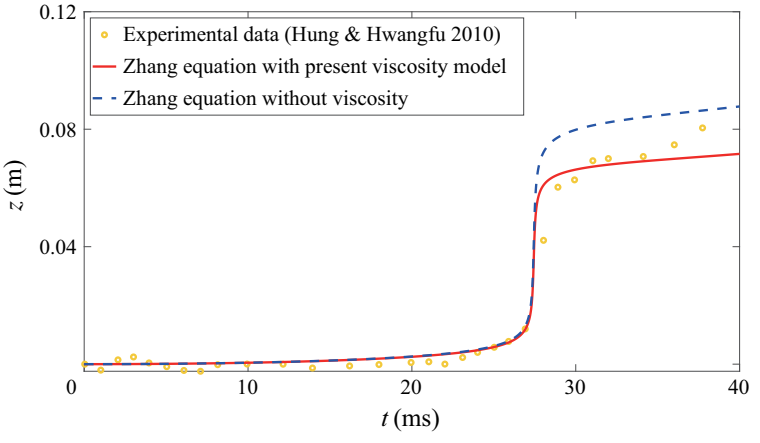


Figure 7. The bubble migration displacement. Yellow dots indicate the experimental data cited from Hung & Hwangfu (2010), the red solid line is given by this model (see § 2), and the blue dashed line is given by the Zhang equation without viscosity ($C_d = 0$).

our theoretical model and those proposed by Levich (1962) and Moore (1963) is presented in figure 8.

Figure 8 graphically illustrates the variation trends of drag coefficients across different models and conditions, along with their comparative disparities. Neither the formulations from Levich (1962) and Moore (1963) nor the analytical solution derived from the spherical assumption in (2.36) can manifest the trend of drag enhancement induced by bubble deformation at elevated Reynolds numbers. At low Reynolds numbers, (2.36) and (2.47) exhibit remarkable congruence with the formulations of Levich and Moore, whereas Moore's equation (2.42) demonstrates a marked departure even under minimal Reynolds number conditions. This limitation is explicitly acknowledged in Moore (1963), wherein (2.42) is specified to be applicable exclusively to higher Reynolds number regimes. To elucidate the discrepancies between (2.36), (2.47) and $C_d = 48/Re$ more intuitively, this analysis employs an alternative vantage point. Using $C_d = 48/Re$ as the benchmark,

https://doi.org/10.1017/jfm.2026.11252 Published online by Cambridge University Press

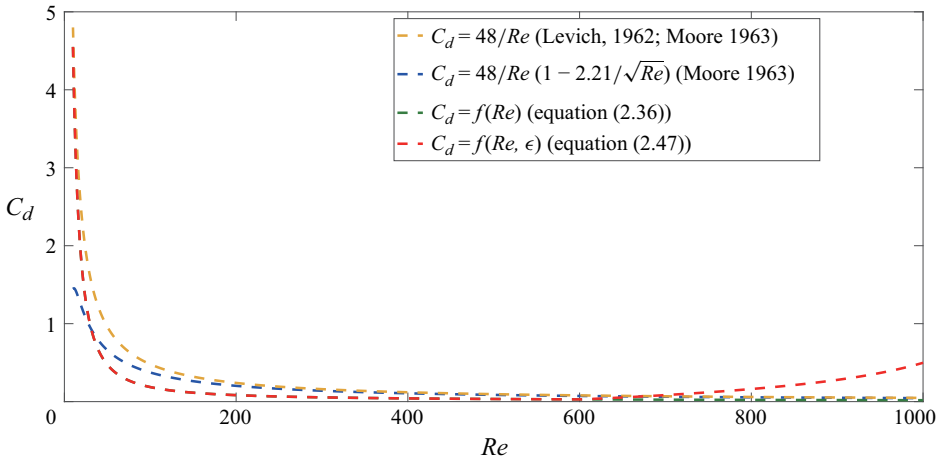


Figure 8. The relationship between C_d and Re.

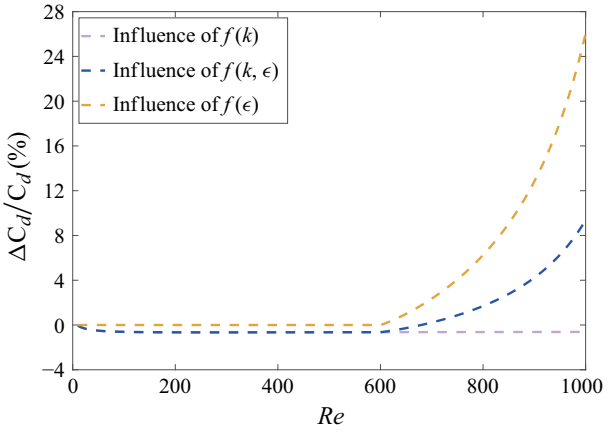


Figure 9. The individual and coupled influences on C_d of the parametric modifications concerning k and ϵ.

the discrepancy magnitude $\Delta C_d/C_d = (C_d^* - C_d)/C_d$ is computed, where C_d^* is the drag coefficient besides benchmark. This approach distinctly reveals the individual and coupled influences of the parametric modifications concerning k and ϵ, as graphically delineated in figure 9.

Figure 9 reveals that as $Re \to 0$, the influences of both k and ϵ become negligible. Under low-Reynolds-number conditions, the effect of k manifests first, further diminishing the drag coefficient. At elevated Reynolds numbers, where bubbles undergo substantial deformation, ϵ predominantly governs the behaviour. Greater deviations from spherical deformation correlate with accelerated increases in drag coefficient. When considering the combined influence of k and ϵ, their counteracting effects result in composite behaviour: at lower Reynolds numbers, the collective influence aligns with that of k, while at higher Reynolds numbers, it converges to an intermediate state that nevertheless manifests in the same manner as ϵ.

https://doi.org/10.1017/jfm.2026.11252 Published online by Cambridge University Press

3.3. *The velocity field around the bubble*

During the initial development of the theoretical model for bubble dynamics, we concurrently derived a simplified particular solution for the velocity field of the Navier–Stokes equation governing fluid around the bubble under axisymmetric conditions. It is worth noting that the solution is unsuitable for describing the velocity fluid around bubble for large Reynolds numbers where the bubble moves rapidly relative to the fluid. It is obvious that the fluid on the bubble surface will become free-slip due to the viscosity for the gas being much less than that for the fluid, while the solution represents the no-slip condition as $u_\theta = v\sin\theta$ at $r = R$. This solution extends (2.21) by incorporating the potential fluid velocity. It is noteworthy that within the axisymmetric model spanning 0 to π and π to 2π, the arithmetic square root fails to capture the antisymmetric nature of tangential velocity. Therefore, the tangential velocity field should be accurately formulated as

$$u_\theta = v\sqrt{\frac{R}{2r}\left(1-\frac{R^2}{r^2}\right)+\left(\frac{3}{4}+\frac{R^3}{4r^3}\right)\frac{R^3}{r^3}\sin^2\theta} \quad (0<\theta<\pi), \tag{3.1a}$$

$$u_\theta = -v\sqrt{\frac{R}{2r}\left(1-\frac{R^2}{r^2}\right)+\left(\frac{3}{4}+\frac{R^3}{4r^3}\right)\frac{R^3}{r^3}\sin^2\theta} \quad (\pi<\theta<2\pi), \tag{3.1b}$$

while for $\theta = 0$ $(\theta = 2\pi)$ and $\theta = \pi$, by superposing the limits of (3.1*a*) and (3.1*b*), we obtain $u_\theta(0) = u_\theta(\pi) = u_\theta(2\pi) = 0$. Notwithstanding this mathematical discrepancy, when employing (2.21) in our preceding analysis, the associated integrals conform to the boundary conditions of 0 to π as lower and upper limits. Through axisymmetric rotation, the corresponding full integrals are derived without compromising the accuracy of pressure, drag force or other computational outcomes. We believe that (3.1*a*) and (3.1*b*), when combined with known laminar special solutions (such as Couette flow or Poiseuille flow), can collectively enrich the analytical solutions of the Navier–Stokes equation. This advancement holds promise for offering valuable reference and renewed impetus in the quest for the general solution of the Navier–Stokes equation, which is one of the seven 'Millennium Prize Problems' in mathematical physics.

Concurrently, we reiterate that the solution presented in (3.1*a*) and (3.1*b*) satisfies the Navier–Stokes equation, yet it does not rigorously fulfil the continuity equation ($\mathrm{div}\,\boldsymbol{u}_v = 0$). This discrepancy arises because our model neglects flow separation (Hain, Kähler & Radespiel 2009), which means that viscous flow exerts no displacement effect, thereby contributing zero to radial velocity. Consequently, the result from (3.1*a*) and (3.1*b*) manifests exclusively as viscous resistance along the direction of flow circumvention. In contrast to Stokes' solution, our formulation incorporates the influence of the convection term, which is a nonlinear component, albeit with minor significance under low-Reynolds-number conditions. Precisely by accounting for this convection term, the velocity field exhibits a spatial square root relationship. This critical inclusion thereby eliminates the Stokes solution's limitation of being applicable solely under extremely-low-Reynolds-number conditions ($Re \ll 1$).

4. Conclusion

Based on the framework of the Zhang equation, the study establishes a theoretical model for the bubble dynamics under dynamic Reynolds numbers. A generalised, time-dependent expression for the drag coefficient C_d is derived to characterise viscous effects. By introducing the relationship between the boundary layer and the bubble size, expressed

https://doi.org/10.1017/jfm.2026.11252 Published online by Cambridge University Press

as $k = 1 + \delta/R$, the model achieves a continuous description under dynamic Reynolds number conditions incorporating boundary layer effects. This formulation elucidates the evolution of C_d with respect to both time and Reynolds number.

Through Helmholtz decomposition, the model analytically resolves the viscous velocity field and the pressure gradient around the bubble under dynamic Reynolds numbers. Crucially, this approach eliminates the empirical constants required in previous potential flow models, offering a more direct description of viscous influences. To enhance accuracy during the high-Reynolds-number phase, the model incorporates a geometric coefficient ϵ to account for non-spherical bubble deformation. This advancement deepens the understanding of the physical mechanisms governing bubble migration under viscous effects, particularly the role of viscous stresses in bubble migration.

The fluid viscosity significantly influences bubble migration while having a minimal effect on bubble oscillation. The derived C_d shows good agreement with the relation $C_d = 48/Re$ proposed by Levich and Moore. With higher bubble migration velocities, a non-spherical correction is introduced via a dimensionless parameter related to bubble deformation, clarifying the impact of frontal area on viscous drag. Comparisons with experimental data demonstrate that the theoretical model predicts the bubble migration trajectories more effectively.

Acknowledgements. The authors are deeply indebted to Professor Y.-L. Liu and Professor S. Li from Harbin Engineering University for giving valuable comments on this work.

Funding. This work is funded by the National Natural Science Foundation of China (52525102, 52088102).

Declaration of interests. The authors report no conflict of interest.

Appendix A. The derivation of the drag coefficient for Stokes' solution

In low-Reynolds-number flows, the convective terms in the Navier–Stokes equations become negligible in comparison to the dissipative terms, hence these terms may be neglected. Under steady flow conditions, the Navier–Stokes equations thus reduce to

$$\mu \nabla^2 \boldsymbol{u} - \boldsymbol{\nabla} p = 0. \tag{A1}$$

Taking the curl of (A1) yields

$$\nabla^2 (\boldsymbol{\nabla} \times \boldsymbol{u}) = \boldsymbol{0}. \tag{A2}$$

If the solid sphere moves at velocity v relative to the fluid, then the velocity field of this situation can be solved by (A2) as

$$u_r = v \cos\theta \left(\frac{3R}{2r} - \frac{R^3}{2r^3} \right), \tag{A3a}$$

$$u_\theta = v \sin\theta \left(\frac{3R}{4r} + \frac{R^3}{4r^3} \right). \tag{A3b}$$

For the spherical bubble, the potential velocity reaches the maximum value at the bubble surface as $v/2$, thus the relative velocity for the viscous field is equal to $v/2$. Then we need to modify (A3a) and (A3b) as

$$u_r = \frac{v}{2} \cos\theta \left(\frac{3R}{2r} - \frac{R^3}{2r^3} \right), \tag{A4a}$$

$$u_\theta = \frac{v}{2} \sin\theta \left(\frac{3R}{4r} + \frac{R^3}{4r^3} \right). \tag{A4b}$$

https://doi.org/10.1017/jfm.2026.11252 Published online by Cambridge University Press

Based on (A1), the pressure field can be computed as

$$p = p_a - \frac{3\mu R v \cos\theta}{4r^2}, \tag{A5}$$

where p_a is the ambient pressure. Coupled with frictional resistance, by integrating (A5) through the bubble surface, the drag force is derived as

$$D = \oint_{S_b} (p\cos\theta - \sigma_{rr}\cos\theta + \sigma_{r\theta}\sin\theta)\,\mathrm{d}S = 3\pi\mu R v. \tag{A6}$$

Similarly, if we define $Re = 2\rho R v/\mu$ and $C_d = D/[\pi\rho R^2 (v/2)^2/2]$, then

$$C_d = \frac{48}{Re}, \tag{A7}$$

which is the drag coefficient suitable for spherical bubble migration in an incompressible, quasi-steady and low-Reynolds-number fluid. The result of (A7) is equivalent to the theoretical results derived by Levich (1962) and Moore (1963), which neglected the convection term.

References

Ai, X. & Ni, B. 2017 Influence of viscosity and surface tension of fluid on the motion of bubbles. *Acta Phys. Sin.* **66** (23), 234702.

Apfel, R.E. 1981 7. Acoustic cavitation. In *Methods in Experimental Physics*, vol. 19, pp. 355–411. Elsevier.

Aybers, N.M. & Tapucu, A. 1969 Studies on the drag and shape of gas bubbles rising through a stagnant liquid. *Wärme – und Stoffübertragung* **2** (3), 171–177.

Best, J.P. 1991 The dynamics of underwater explosions. PhD thesis, University of Wollongong, Australia.

Brujan, E.A., Pearson, A. & Blake, J.R. 2005 Pulsating, buoyant bubbles close to a rigid boundary and near the null final Kelvin impulse state. *Intl J. Multiphase Flow* **31** (3), 302–317.

Brujan, E.-A., Zhang, A.-M., Liu, Y.-L., Ogasawara, T. & Takahira, H. 2022 Jetting and migration of a laser-induced cavitation bubble in a rectangular channel. *J. Fluid Mech.* **948**, A6.

De Graaf, K.L., Brandner, P.A. & Penesis, I. 2014 Bubble dynamics of a seismic airgun. *Exp. Therm. Fluid Sci.* **55**, 228–238.

Fang, X.-L., Wang, P.-P., Meng, Z.-F., Ming, F.-R. & Zhang, A-M. 2025*a* An accurate thermodynamic Riemann-SPH model for multiphase flows with applications in bubble dynamics. *J. Comput. Phys.* **533**, 113969.

Fang, X.-L., Wang, P.-P., Meng, Z.-F., Ming, F.-R. & Zhang, A-M. 2025*b* A low-dissipation and accurate Riemann SPH for multiphase flows with large density ratios and strong shocks. *J. Comput. Phys.* **539**, 114210.

Fogler, S. 1969 The influence of reacting gases on the motion of collapsing cavities. *Chem. Engng Sci.* **24** (7), 1043–1054.

Fry, F.J., Sanghvi, N.T., Foster, R.S., Bihrle, R. & Hennige, C. 1995 Ultrasound and microbubbles: their generation, detection and potential utilization in tissue and organ therapy – experimental. *Ultrasound Med. Biol.* **21** (9), 1227–1237.

Gilmore, F.R. 1952 *The Growth or Collapse of a Spherical Bubble in a Viscous Compressible Liquid*, California Institute of Technology.

Hain, R., Kähler, C.J. & Radespiel, R. 2009 Dynamics of laminar separation bubbles at low-Reynolds-number aerofoils. *J. Fluid Mech.* **630**, 129–153.

Han, L., Yan, S. & Li, S. 2024 Theoretical investigation of spherical bubble dynamics in high Mach number regimes. *J. Mar. Sci. Appl.* **23** (1), 39–48.

Hanafizadeh, P., Karbalaee, M.S., Sharbaf, E.B. & Ghanbarzadeh, S. 2013 Drag coefficient and Strouhal number analysis of cylindrical tube in two phase flow. *Energy Equipment Syst.* **1** (1), 35–58.

Hicks, A.N. 1970 Effect of bubble migration on explosion-induced whipping in ships. Naval Ship Research and Development Center Technical Report 3301.

Hung, C.F. & Hwangfu, J.J. 2010 Experimental study of the behaviour of mini-charge underwater explosion bubbles near different boundaries. *J. Fluid Mech.* **651**, 55–80.

Keller, J.B. & Miksis, M. 1980 Bubble oscillations of large amplitude. *J. Acoust. Soc. Am.* **68** (2), 628–633.

https://doi.org/10.1017/jfm.2026.11252 Published online by Cambridge University Press

KLIBANOV, A.L. 2007 Ultrasound molecular imaging with targeted microbubble contrast agents. *J. Nucl. Cardiol.* **14** (6), 876–884.
KONG, G., MIRSANDI, H., BUIST, K.A., PETERS, E.A.J.F., BALTUSSEN, M.W. & KUIPERS, J.A.M. 2019 Oscillation dynamics of a bubble rising in viscous liquid. *Exp. Fluids* **60** (8), 130.
LEE, J.S., WEON, B.M., PARK, S.J., JE, J.H., FEZZAA, K. & LEE, W.-K. 2011 Size limits the formation of liquid jets during bubble bursting. *Nat. Commun.* **2** (1), 367.
LEVI, E. 1983 A universal Strouhal law. *J. Engng Mech.* **109** (3), 718–727.
LEVICH, W.G. 1962 *Physicochemical Hydrodynamics*, pp. 396–402. Prentice-Hall, Inc.
LI, S., VAN DER MEER, D., ZHANG, A-M., PROSPERETTI, A. & LOHSE, D. 2020 Modelling large scale airgun-bubble dynamics with highly non-spherical features. *Intl J. Multiphase Flow* **122**, 103143.
LI, S., SUN, L.Q. & ZHANG, A-M. 2014 Dynamic behavior of rising bubble. *Acta Phys. Sin.* **63** (18), 287–299.
LIOUMBAS, J.S. & KARAPANTSIOS, T.D. 2015 Bubble dynamics and substrate thermalization during boiling in water saturated porous matrix. *Exp. Therm. Fluid Sci.* **67**, 75–80.
LIU, N.-N., ZHANG, A., CUI, P., WANG, S.-P. & LI, S. 2021 Interaction of two out-of-phase underwater explosion bubbles. *Phys. Fluids* **33** (10), 106103.
LOHSE, D., SCHMITZ, B. & VERSLUIS, M. 2001 Snapping shrimp make flashing bubbles. *Nature* **413** (6855), 477–478.
LOTH, E. 2008 Quasi-steady shape and drag of deformable bubbles and drops. *Intl J. Multiphase Flow* **34** (6), 523–546.
MA, J., HSIAO, C.-T. & CHAHINE, G.L. 2018 Numerical study of acoustically driven bubble cloud dynamics near a rigid wall. *Ultrasonics Sonochem.* **40**, 944–954.
MATTSON, M. & MAHESH, K. 2011 Simulation of bubble migration in a turbulent boundary layer. *Phys. Fluids* **23** (4), 045107.
MEROUANI, S. & HAMDAOUI, O. 2016 The size of active bubbles for the production of hydrogen in sonochemical reaction field. *Ultrasonics Sonochem.* **32**, 320–327.
MITROVIC, J. 1998 Nucleate boiling of refrigerant–oil mixtures: bubble equilibrium and oil enrichment at the interface of a growing vapour bubble. *Intl J. Heat Mass Transfer* **41** (22), 3451–3467.
MOORE, D.W. 1963 The boundary layer on a spherical gas bubble. *J. Fluid Mech.* **16** (2), 161–176.
PEÑAS-LÓPEZ, P., PARRALES, M.A., RODRÍGUEZ-RODRÍGUEZ, J. & VAN DER MEER, D. 2016 The history effect in bubble growth and dissolution. Part 1. Theory. *J. Fluid Mech.* **800**, 180–212.
PLESSET, M.S. 1949 The dynamics of cavitation bubbles. *ASME J. Appl. Mech.* **16** (3), 277–282.
PLESSET, M.S. 1964 Bubble dynamics. In *Cavitation in Real Liquids* (ed. R. Davies). Elsevier.
PLESSET, M.S. & PROSPERETTI, A. 1977 Bubble dynamics and cavitation. *Annu. Rev. Fluid Mech.* **9**, 145–185.
PROSPERETTI, A. & LEZZI, A. 1986 Bubble dynamics in a compressible liquid. Part 1. First-order theory. *J. Fluid Mech.* **168**, 457–478.
RAVELET, F., COLIN, C. & RISSO, F. 2011 On the dynamics and breakup of a bubble rising in a turbulent flow. *Phys. Fluids* **23** (10), 103301.
RAYLEIGH, LORD 1917 VIII. On the pressure developed in a liquid during the collapse of a spherical cavity. *Phil. Mag.* **6** (34), 94–98.
ROGHAIR, I., LAU, Y.M., DEEN, N.G., SLAGTER, H.M., BALTUSSEN, M.W., ANNALAND, M.V.S. & KUIPERS, J.A.M. 2011 On the drag force of bubbles in bubble swarms at intermediate and high Reynolds numbers. *Chem. Engng Sci.* **66** (14), 3204–3211.
ROIG, V., ROUDET, M., RISSO, F. & BILLET, A.-M. 2012 Dynamics of a high-Reynolds-number bubble rising within a thin gap. *J. Fluid Mech.* **707**, 444–466.
SABDENOV, K.O. 2020 Gas bubble dynamics in a fluid with chemical reactions. *Combust. Explos. Shock Waves* **56** (3), 271–277.
VEGA-MARTÍNEZ, P., ENRÍQUEZ, O.R. & RODRÍGUEZ-RODRÍGUEZ, J. 2017 Some topics on the physics of bubble dynamics in beer. *Beverages* **3** (3), 38.
VERSCHOOF, R.A., VAN DER, VEEN, R., C.A., SUN, C. & LOHSE, D. 2016 Bubble drag reduction requires large bubbles. *Phys. Rev. Lett.* **117** (10), 104502.
WANG, Q. 2016 Local energy of a bubble system and its loss due to acoustic radiation. *J. Fluid Mech.* **797**, 201–230.
WANG, X., WU, G., ZHENG, X., DU, X. & ZHANG, Y. 2022 Theoretical investigation and experimental support for the cavitation bubble dynamics near a spherical particle based on Weiss theorem and Kelvin impulse. *Ultrasonics Sonochem.* **89**, 106130.
YAN, X., JIA, Y., WANG, L. & CAO, Y. 2017 Drag coefficient fluctuation prediction of a single bubble rising in water. *Chem. Engng J.* **316**, 553–562.

https://doi.org/10.1017/jfm.2026.11252 Published online by Cambridge University Press

YANG, W.-J. & YEH, H.-C. 1966 Theoretical study of bubble dynamics in purely viscous fluids. *AIChE J.* **12** (5), 927–931.

ZENIT, R. & RODRÍGUEZ-RODRÍGUEZ, J. 2018 The fluid mechanics of bubbly drinks. *Phys. Today* **71** (11), 44–50.

ZHANG, A-M., CUI, P., CUI, J. & WANG, Q.X. 2015 Experimental study on bubble dynamics subject to buoyancy. *J. Fluid Mech.* **776**, 137–160.

ZHANG, A-M., LI, S.-M., CUI, P., LI, S. & LIU, Y.-L. 2023 A unified theory for bubble dynamics. *Phys. Fluids* **35** (3), 033323.

ZHANG, A-M., LI, S.-M., XU, R.-Z., PEI, S.-C., LI, S. & LIU, Y.-L. 2024 A theoretical model for compressible bubble dynamics considering phase transition and migration. *J. Fluid Mech.* **999**, A58.

ZHANG, Y.L., YEO, K.S., KHOO, B.C. & WANG, C. 2001 3-D jet impact and toroidal bubbles. *J. Comput. Phys.* **166** (2), 336–360.

https://doi.org/10.1017/jfm.2026.11252 Published online by Cambridge University Press